

The magnetic field and dust filaments in the Polaris Flare

G. V. Panopoulou,^{1,2*} I. Psaradaki,¹ K. Tassis^{1,2}

¹*Department of Physics and ITCP†, University of Crete, 71003, Heraklion, Greece*

²*Foundation for Research and Technology - Hellas, IESL, Voutes, 71110 Heraklion, Greece*

Accepted XXX. Received YYY; in original form ZZZ

ABSTRACT

In diffuse molecular clouds, possible precursors of star-forming clouds, the effect of the magnetic field is unclear. In this work we compare the orientations of filamentary structures in the Polaris Flare, as seen through dust emission by *Herschel*, to the plane-of-the-sky magnetic field orientation (B_{pos}) as revealed by stellar optical polarimetry with RoboPol. Dust structures in this translucent cloud show a strong preference for alignment with B_{pos} . 70% of field orientations are consistent with those of the filaments (within 30°). We explore the spatial variation of the relative orientations and find it to be uncorrelated with the dust emission intensity and correlated to the dispersion of polarization angles. Concentrating in the area around the highest column density filament, and in the region with the most uniform field, we infer the B_{pos} strength to be $24 - 120 \mu\text{G}$. Assuming that the magnetic field can be decomposed into a turbulent and an ordered component, we find a turbulent-to-ordered ratio of $0.2 - 0.8$, implying that the magnetic field is dynamically important, at least in these two areas. We discuss implications on the 3D field properties, as well as on the distance estimate of the cloud.

Key words: ISM: magnetic fields – ISM: structure – ISM: clouds – ISM: individual objects: Polaris Flare – polarization

1 INTRODUCTION

The structure of interstellar clouds is highly complex, characterized by the existence of elongations, or filaments, of various scales (e.g. Myers 2009). The Gould Belt Survey conducted by the *Herschel* space observatory captured the morphologies of the nearby molecular clouds with unprecedented sensitivity and detail, allowing the study of filamentary structures to advance (e.g. André et al. 2010). A better understanding of filament properties and their relation to their environments could provide clues as to how clouds proceed to form stars.

To this end, important questions to answer are whether the magnetic field interacts with filaments and how this interaction takes place. Its role in the various stages and environments of star formation is hotly debated. In simulations of super-Alfvénic turbulence, magnetic fields are tangled due to the gas flow (e.g. Ostriker, Stone, & Gammie 2001; Falceta-Gonçalves et al. 2008). In such models, filaments are formed by shock interactions (Heitsch et al. 2001; Padoan et al. 2001) and the magnetic field within

them is found to lie along their spines (Heitsch et al. 2001; Ostriker, Stone, & Gammie 2001; Falceta-Gonçalves et al. 2008). In studies of sub/trans-Alfvénic turbulence, where the magnetic field is dynamically important, filament orientations with respect to the large scale ordered field, depend on whether gravity is important. In simulations where gravity is not taken into account (e.g. Falceta-Gonçalves et al. 2008) or structures are gravitationally unbound (Soler et al. 2013), filaments are parallel to the magnetic field. On the other hand, self-gravitating elongated structures are perpendicular to the magnetic field (Mouschovias 1976; Nakamura & Li 2008; Soler et al. 2013). Both configurations are the result of the magnetic force facilitating flows along field lines. Finally, if the magnetic field surrounding a filament has a helical configuration (Fiege & Pudritz 2002) the relative orientation of the two as projected on the plane of the sky can have any value, depending on projection, curvature and if the field is mostly poloidal or toroidal (Matthews 2001).

The relation between cloud structure and the magnetic field was highlighted early on by observational studies (e.g. in the Pleiades, Hall 1955). On cloud scales, Li et al. (2013) found that the distribution of relative orientations of elongated clouds and the magnetic field (both projected on the plane of the sky) is bimodal: clouds either tend to be par-

* E-mail: panopg@physics.uoc.gr

† Institute for Theoretical and Computational Physics, formerly Institute for Plasma Physics

allel or perpendicular (in projection) to the magnetic field. In a series of papers the *Planck* collaboration compared the magnetic field to ISM structure across a range of hydrogen column densities (N_{H}). [Planck Collaboration Int. XXXII \(2014\)](#) considered the orientation of structures in the diffuse ISM in the range of $N_{\text{H}} \sim 10^{20} - 10^{22}$ and found significant alignment with the plane-of-the-sky magnetic field (B_{pos}). [Planck Collaboration Int. XXXV \(2015\)](#) found that in their sample of 10 nearby clouds, substructure at high column density tends to be perpendicular to the magnetic field, whereas at low column density there is a tendency for alignment.

Studies of optical and NIR polarization, tracing B_{pos} in cloud envelopes, show that dense filaments within star-forming molecular clouds tend to be perpendicular to the magnetic field ([Pereyra & Magalhães 2004](#); [Alves et al. 2008](#); [Chapman et al. 2011](#); [Sugitani et al. 2011](#)). On the other hand, there are diffuse linear structures termed *striations*, that share a common smoothly varying orientation and are situated either in the outskirts of clouds ([Goldsmith et al. 2008](#); [Alves de Oliveira et al. 2014](#)) or near dense filaments ([Palmeirim et al. 2013](#)). These structures show alignment with B_{pos} ([van den Bergh 1956](#); [Chapman et al. 2011](#); [Palmeirim et al. 2013](#); [Alves de Oliveira et al. 2014](#); [Malinen et al. 2015](#)). The extremely well-sampled data of [Franco & Alves \(2015\)](#) in Lupus I show that B_{pos} is perpendicular to the cloud's main axis but parallel to neighbouring diffuse gas. There are, however, exceptions to this trend (e.g. L1506 in Taurus, [Goodman et al. 1990](#)).

While the large-scale magnetic field has been mapped in many dense molecular clouds, little is known about the field in translucent molecular clouds. In this paper we investigate the relation of the magnetic field to the gas in the Polaris Flare, a high-latitude diffuse cloud. This molecular cloud extends above the galactic plane and is at an estimated distance between 140 and 240 pc, although this is debated (e.g. [Zagury et al. 1999](#); [Schlafly et al. 2014](#)). It is a translucent region ($A_{\text{V}} \lesssim 1$ mag, [Cambrésy et al. 2001](#)) devoid of star formation activity ([André et al. 2010](#); [Men'shchikov et al. 2010](#); [Ward-Thompson et al. 2010](#)), except for the existence of possibly prestellar core(s) in the densest part of the cloud MCLD 123.5+24.9 (MCLD123) ([Ward-Thompson et al. 2010](#); [Wagle et al. 2015](#)). Signatures of intense velocity shear have been identified in this region and have been linked to the dissipation of supersonic (but trans-Alfvénic) turbulence ([Hily-Blant & Falgarone 2009](#), and references therein).

The dust emission in ~ 16 deg² of the Polaris Flare has been mapped by *Herschel* ([Pilbratt et al. 2010](#)) as part of the *Herschel* Gould Belt Survey ([André et al. 2010](#); [Miville-Deschênes et al. 2010](#); [Men'shchikov et al. 2010](#); [Ward-Thompson et al. 2010](#)). The *Planck* space observatory has provided the first map of the plane-of-the-sky magnetic field in the area at tens of arcminute resolution ([Planck Collaboration Int. XIX 2015](#); [Planck Collaboration Int. XX 2015](#)). In [Panopoulou et al. \(2015\)](#) (Paper I) we presented a map of the plane-of-the-sky magnetic field in the same area, measured by stellar optical polarimetry with RoboPol. The resolution of optical polarimetry (pencil beams) and coverage of our data allow for a detailed comparison between magnetic field and cloud

structure. The goal of this work is to compare the magnetic field orientation to that of the linear structures in the Polaris Flare and to estimate the plane-of-the-sky component of the field in various regions of the cloud. In section 2.1 we present the distribution of relative orientations of filaments and B_{pos} throughout the mapped region. We compare properties such as the relative orientations and polarization angle dispersion across the map in section 2.2 and present the distribution of filament widths in section 2.3. We analyse two regions of interest separately in section 2.4 and estimate the B_{pos} strength in these regions in section 2.5. Finally, we discuss implications of our findings in section 3 and summarize our results in section 4.

2 RESULTS

2.1 Relative orientations of B_{pos} and dust filaments

We use the *Herschel*-SPIRE 250 μm map¹ in our analysis of cloud structure. Filamentary structures are evident throughout the *Herschel* image of this translucent cloud. We will compare the orientations of these structures to the optical polarization data presented² in Paper I, shown as line segments on the 250 μm dust emission image in Fig. 1. The segment length is proportional to the (debiased) fractional linear polarization, p_d . A line showing a p_d of 2% is located in the bottom left corner and a line of 1 pc length is located in the top left. We adopt a distance of 150 pc to be consistent with the analysis of *Herschel* data in the literature (based on [Heithausen 1999](#)). The rectangles highlight regions of interest that will be referred to in the following analysis. Insets on the right show zoomed-in versions of both regions. A preliminary inspection of the map shows that the orientation of B_{pos} revealed from optical polarimetry seems to correlate well with the apparent orientations of filaments in most of the map. This correlation can be quantified by measuring the relative orientation of the two.

An excellent tool for determining the orientation of linear structures, irrespective of their brightness, is the Rolling Hough Transform (RHT) ([Clark et al. 2014](#)). It was introduced in the study of diffuse HI and has been used in analyses of molecular clouds as well ([Koch & Rosolowsky 2015](#); [Malinen et al. 2015](#)). The RHT quantifies the linearity of cloud structure for every image pixel. It does so by measuring the intensity along any given direction within a disk region surrounding each pixel. The RHT returns the probability that a pixel is part of a linear structure as a function of angle. Integrating for all angles results in a visualization of linear features in the image (RHT backprojection).

¹ The map is part of the preliminary data available at the *Herschel* Gould Belt Survey archive.

² Following the publication of the catalogue of 609 measurements in Paper I, we discovered an error in the conversion from polarization angle with respect to the North Celestial Pole to angle with respect to the North Galactic Pole. This error affected the orientation of 77 segments in the top of the published map. We corrected the formula used for the conversion and have updated the values of galactic angle in the published catalogue. This updated version is used in this work and can be found at <http://cds.u-strasbg.fr/>. No other changes have been made to the original release.

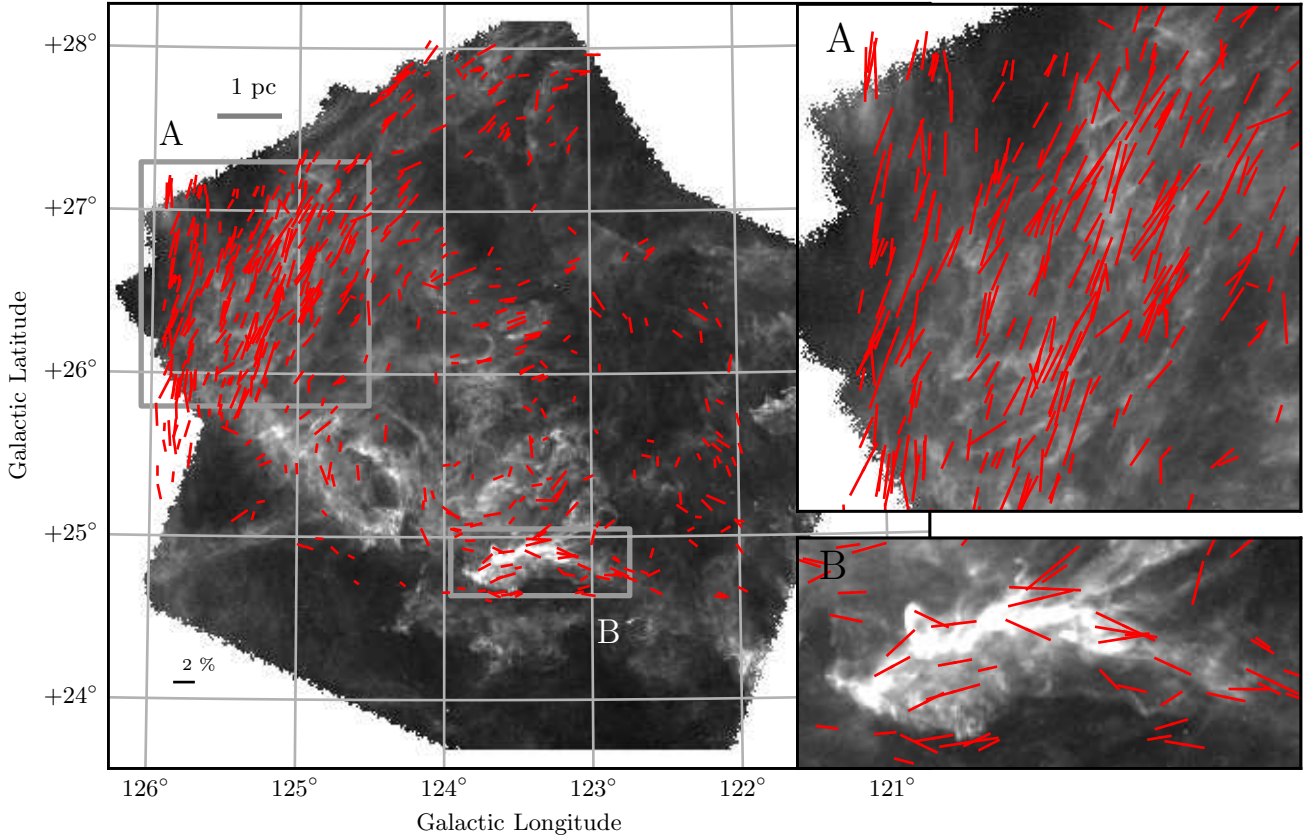


Figure 1. *Herschel* 250 μm image of the Polaris Flare (grayscale). Segments are the optical polarization data from Paper I. Regions A (striations) and B (MCLD123), indicated by the rectangles in the full map, are shown in the top right and bottom right inlets for detail. Scales of 1 pc and $p_d = 2\%$ are shown in the top left and bottom left corners of the full map.

We applied the RHT to the *Herschel* 250 μm image and present the RHT backprojection in Fig. 2. The darkest pixels in the image belong to well-defined linear structures in intensity (filaments and striations). Apart from these structures, the RHT backprojection contains some spurious features, e.g. in the bottom part of the map where dust emission is very faint or absent. These features seem correlated with the *Herschel* scanning direction. Since neither cloud structure nor magnetic field orientation coincide with this direction, the effect of these features on the distribution of relative orientations will be to randomize a very small number (if any) of values, introducing misalignment.

The polarization segments tracing the orientation of B_{pos} are overplotted on the backprojection in Fig. 2. At the position of each polarization measurement, we calculate the mean RHT angle (θ_{RHT} , defined as in Clark et al. 2014), within a circle of diameter 0.17 pc (corresponding to an angular diameter of $4'$). We then compare θ_{RHT} to the orientation of each polarization segment, θ , by taking the absolute value of their difference³, $|\theta - \theta_{\text{RHT}}|$. There are 39 polarization measurements that extend outside the dust

emission image and are not included in the comparison to cloud structures. The distribution of the relative orientations for the 570 remaining measurements is plotted in Fig. 3. There is a strong preference in alignment: 70% of polarization measurements are within 30° of the orientation of linear features in their surrounding gas. A Monte-Carlo run showed that the probability of obtaining this correlation by chance is less than 10^{-6} . Only 8% are within 30° of being perpendicular to their surrounding gas. We explored the effect of changing the parameters of the RHT, as well as the area around each star used in calculating θ_{RHT} , and found no significant variation for a large portion of the parameter space.

2.2 Variation across the field

The results presented above on the alignment of filaments and B_{pos} concerned the entire map. However, both field and cloud structure are not homogeneous across the cloud. For example, there is a low column density area of striations, marked by the rectangle as region A in Fig. 1, where B_{pos} exhibits ordered structure. Adjacent to this area, towards lower latitude and longitude, in a significant portion of the map, measurements are sparse and polarization angles show substantial dispersion.

³ All angles are defined with respect to the North and increase towards the East, according to the IAU convention.

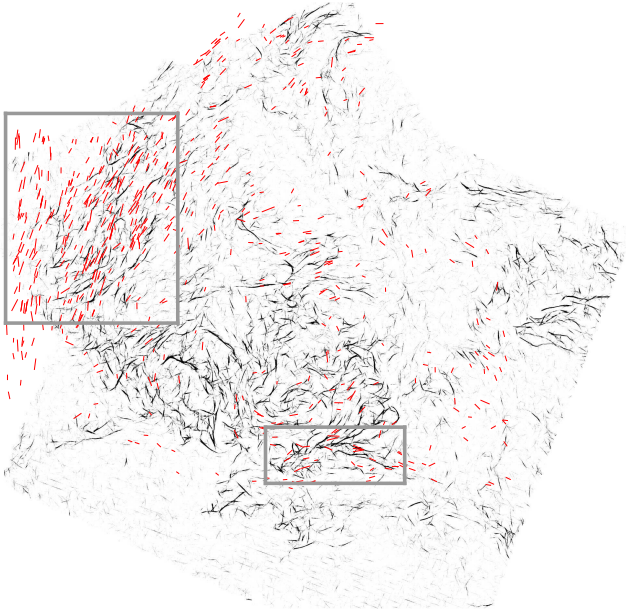


Figure 2. RHT visualization of the *Herschel* 250 μm image of the Polaris Flare (grayscale). Dark pixels correspond to a high probability of linearity. The optical polarization segments from Paper I have been overplotted in red. Regions A and B are outlined as in Fig. 1.

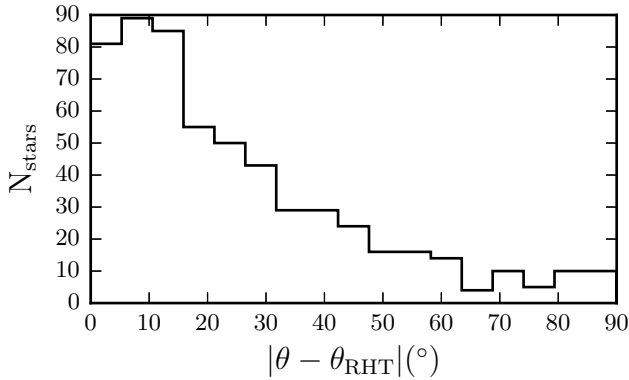


Figure 3. Distribution of the absolute difference between the angle of each polarization segment and the RHT angle in its vicinity ($|\theta - \theta_{\text{RHT}}|$). The distribution contains all 570 polarization measurements that lie in the *Herschel* image.

The various trends existing in the measured cloud properties can be better visualized by constructing maps of average (smoothed) quantities across the sky. The maps are constructed by creating a grid (5' squares) of the field. The value at each grid center is calculated by averaging the values of star measurements within 10' of it. The final map is smoothed using a boxcar filter of 5' width. Fig. 4 shows such maps of various quantities: (a) number of significant stellar polarization measurements ($p_d/\sigma_p \geq 2.5$), (b) *Herschel* 250 μm intensity, (c) polarization angle, θ , (d) scatter of θ , (e) $|\theta - \theta_{\text{RHT}}|$ and (f) p_d . Only bins with at least 5 measurements were used to produce the maps (reducing this number to 3 did not make a qualitative difference).

The number of significant stellar polarization measurements is highest in region A, which is the bright part in the upper left of the map in panel (a). The number density (per 5' bin) in this area is more than twice that in the rest of the map. Smaller local maxima are found: (i) in region B, (ii) in the center of the map ($123.5^\circ, +26.3^\circ$) and (iii) above the striations at ($124.5^\circ, +27.5^\circ$). As noted in Paper I, this variation in the number of measurements is not due to variations in stellar density across the field, or due to systematics such as observing conditions. Panel (b) shows the *Herschel* 250 μm image smoothed with a boxcar filter of 5' width. The MCLD123 filament (region B) stands out as a maximum of intensity. By comparing the number density of significant stellar polarization measurements to the dust emission intensity (panels (a) and (b)) we find that the overall structure of the two maps is significantly different. Therefore, the variation of the density of significant polarization measurements cannot be attributed to variations in the column density.

The average polarization angles in panel (c) are calculated as the circular mean:

$$\bar{\theta} = \frac{1}{2} \arctan \left(\frac{\sum_{i=1}^N \sin(2\theta_i)}{\sum_{i=1}^N \cos(2\theta_i)} \right), \quad (1)$$

where N is the number of measurements in each bin. The average polarization angle defines a number of domains of different orientation throughout the field, separated by abrupt angle changes. The thin dark curves at the edges of some domains are an artefact of the smoothing, they do not represent measurements of 90° . $\bar{\theta}$ seems to rotate clockwise from 160° (bright yellow) in region A, to 40° (blue) below the center of the map.

The scatter of polarization angles $\text{std}(2\theta)$ in panel (d) is measured using the circular standard deviation:

$$\text{std}(2\theta) = \sqrt{-2 \ln \left(\sqrt{\left(\frac{1}{N} \sum_{i=1}^N \sin 2\theta_i \right)^2 + \left(\frac{1}{N} \sum_{i=1}^N \cos 2\theta_i \right)^2} \right)}. \quad (2)$$

The values obtained by this equation do not represent the dispersion that would characterize a normal distribution of angles. They only serve for comparison between the various areas of the map. The bright regions in panel (d) (large standard deviations) correspond to regions with very few measurements, as can be seen by comparing with panel (a). Region A and an area with $\text{std}(2\theta) < 30^\circ$ in the center of the map stand out as the areas with lowest dispersion.

The relative orientation of B_{pos} and the filamentary structures in the cloud, shown in panel (e), is very similar to the $\text{std}(2\theta)$ map. Regions characterized by a large polarization angle dispersion appear to coincide with regions where filaments are perpendicular to B_{pos} . The preference in alignment throughout the map, seen in Fig. 3, is evident, as regions with $|\theta - \theta_{\text{RHT}}| \lesssim 20^\circ$ (dark) occupy most of the map area.

The highest values of p_d (panel f) are in the region of the striations. The *Planck* polarized intensity peak coincides with the brightest part of this map at ($126^\circ, +27^\circ$) (see figure A.1. in [Planck Collaboration Int. XX 2015](#)). The second, but lower, local maximum in p_d is in region B. The

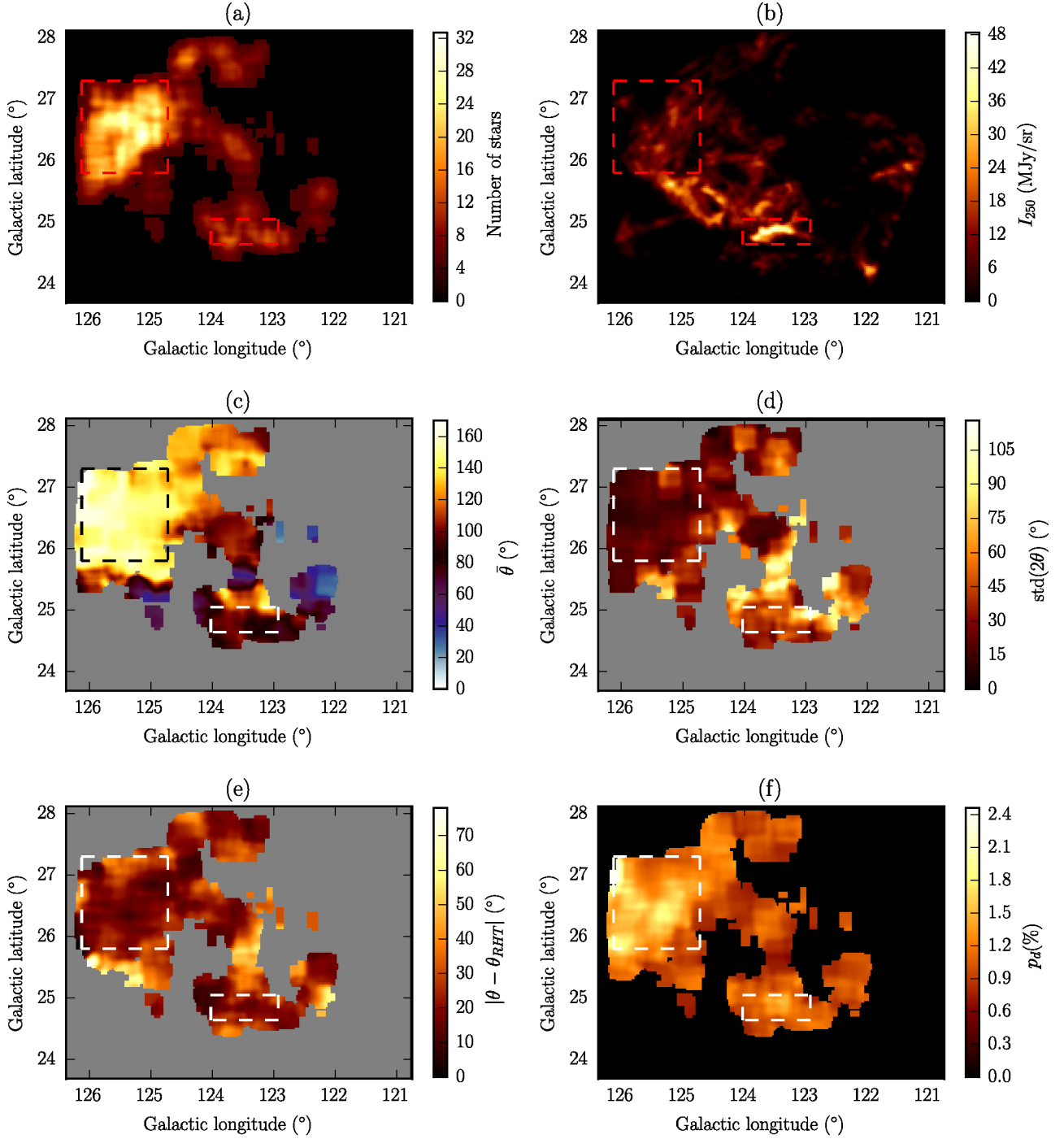


Figure 4. Quantities smoothed on a $5' \times 5'$ grid: (a) number of stellar polarization measurements, (b) *Herschel* 250 μm intensity, (c) polarization angle, (d) polarization angle scatter, (e) relative orientation of B_{pos} and filaments, (f) fractional linear polarization. Rectangles outline regions A and B.

spatial variation of p_d resembles that of N_{stars} . This correlation is evident in Fig. 5 (top left), where the average value of N_{stars} is plotted for each (equally-populated with pixels) p_d bin. This correlation is natural, since the polarization measurements were selected in Paper I to satisfy $p_d/\sigma_p \geq 2.5$. Since the observational errors σ_p are uniform across the field (Paper I), it is more likely that a larger number of significant measurements will be obtained in regions of higher p_d .

Additional support to the fact that the variation in the

number of significant polarization measurements is uncorrelated with the column density is given by the plot on the top right panel of Fig. 5, where the visual extinction, A_V , (from the map of [Cambr  s et al. 2001](#)) is plotted against p_d (from panel f, Fig. 4). One possibility that explains the observed variation of N_{stars} is that the 3D orientation of the magnetic field varies significantly throughout the sky. If this is true, then it is expected that more significant polarization will be detected in regions where the field is mostly on the

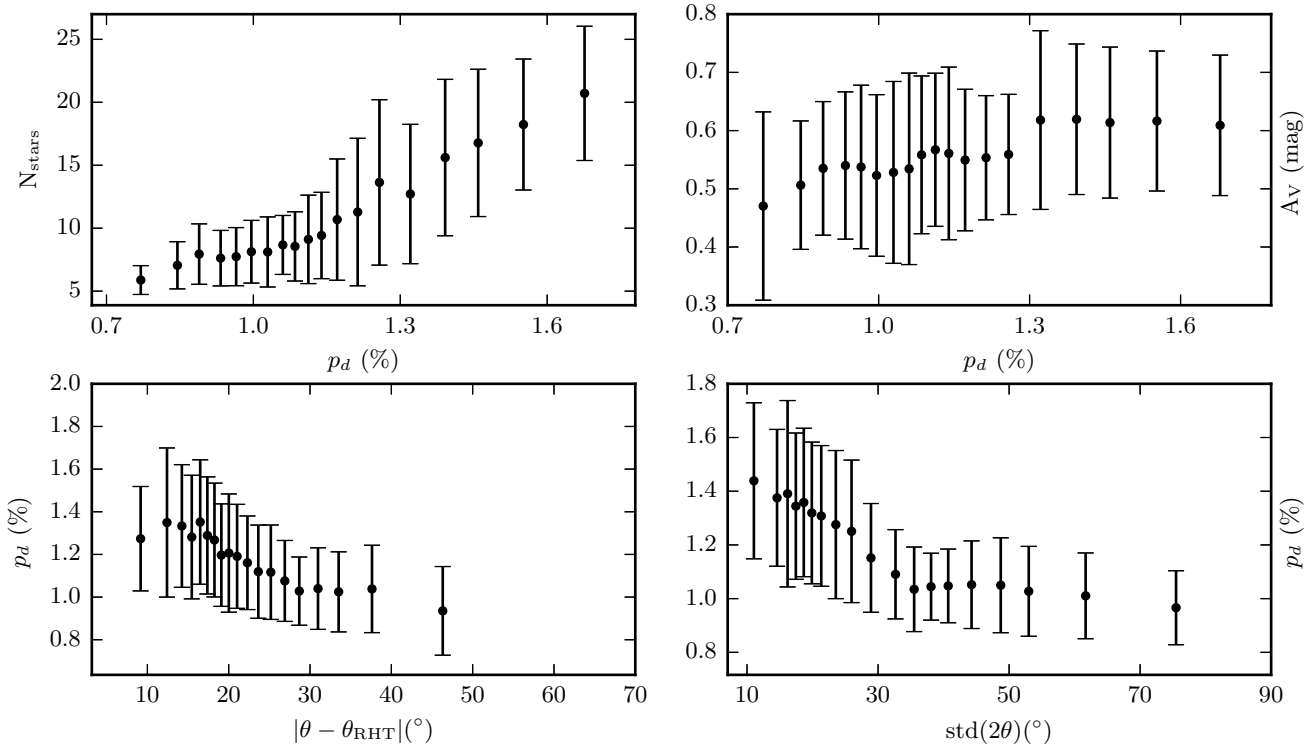


Figure 5. Binned pixel-to-pixel comparison of maps from Fig. 4. Top left: N_{stars} versus p_d , top right: extinction A_V versus p_d , bottom left: p_d versus $|\theta - \theta_{\text{RHT}}|$, bottom right: p_d versus $\text{std}(\theta)$. Errorbars show the $\pm 1\sigma$ from the mean in each bin. Bins contain the same number of pixels.

plane of the sky. In these regions, p_d should be higher and this is consistent with the correlation of p_d and N_{stars} that we find. Also, if the field strength is more significant than turbulent gas motions, which tend to randomize its orientation (see section 2.5), regions where B_{pos} is stronger (high p_d , N_{stars}) should have a small angle scatter. This is indeed the case as can be seen in the bottom right panel of Fig. 5. However, a significant contribution to this trend is likely to be coming from the larger measurement error of lower-significance measurements (near the cut of $p_d/\sigma_p \geq 2.5$).

If the assumption of a strong magnetic field holds, then, diffuse, non self-gravitating filaments such as the ones in this cloud are expected to be mostly parallel to the 3D field orientation. So, if the field lies mostly on the plane of the sky, the alignment of the projected field and filaments will be easily detected. If, though, the field is mostly along the line-of-sight, filaments and field can be observed as having any relative orientation. A hint of such a trend may exist in the bottom left panel of Fig. 5. Planck Collaboration Int. XXXII (2014) find this exact trend (their figure 13) and attribute it to the same effect: the projection of the 3D field on the sky. The anti-correlation of p_d with $\text{std}(\theta)$ is also observed (figure 21 of Planck Collaboration Int. XIX 2015).

Planck Collaboration Int. XXXII (2014) also find that the degree of alignment decreases with column density in the range $N_H = [10^{20}, 10^{22}] \text{ cm}^{-2}$. In contrast to this, it is evident even visually that panels (b) and (e) in Fig. 4 are uncorrelated – we see no sign of such a trend. It is possible that the range of column densities in the Polaris Flare is significantly different than that in the work

of Planck Collaboration Int. XXXII (2014). To investigate whether this is the case, we convert the range of A_V in the Polaris Flare to N_H using the standard relation of Bohlin et al. (1978): $N_H = 1.9 \times 10^{21} A_V (\text{cm}^{-2}/\text{mag})$. From the A_V map of Cambr  sy et al. (2001) values in the cloud vary within: $A_V = [0.2, 1.2] \text{ mag} \Rightarrow N_H = [0.4, 2.3] \times 10^{21} \text{ cm}^{-2}$. Because the Cambr  sy et al. (2001) data have a rather low resolution ($8'$), this range may be underestimated. Indeed, the cores in MCLD123 have $N_H \sim 10^{22} \text{ cm}^{-2}$. Therefore, the range of N_H in the cloud is comparable to that of Planck Collaboration Int. XXXII (2014). In their paper, the Planck collaboration infer that the anti-correlation of alignment with column density is most likely due to the existence of molecular cloud structures that are perpendicular to the magnetic field. The only available explanation for this observation is that matter in magnetically-dominated self-gravitating clouds collapses preferentially along field lines, producing structures that are elongated and perpendicular to the field. If we accept this reasoning, it should not come as a surprise that we do not find such a trend in the gravitationally unbound Polaris Flare.

In summary, the above correlations seem to indicate the presence of a strong magnetic field in the cloud which may change orientation from being mostly parallel to the plane-of-the-sky in region A to being more inclined in other areas.

2.3 Filament widths

An important morphological characteristic of filaments is their width. We use the Filament Trait-Evaluated Recon-

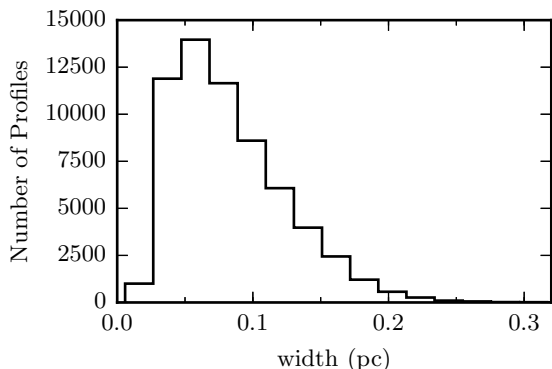


Figure 6. Distribution of widths along filaments in the *Herschel* image.

struction (FiLTER) method⁴ (Panopoulou et al. 2014) to construct the width distribution of filaments in the *Herschel* image. FiLTER takes as input the skeleton of an image and finds the width of the elongated structures. For this purpose, a Gaussian is fit to the radial profile at every point along the filament axis, and the resulting FWHM is deconvolved by the beam size. The skeleton is produced by DisPerSe (Sousbie 2011) which is a topological code that can extract the filamentary structures of an image. It is designed to connect local maxima (cores). This property renders the construction of a representative skeleton difficult, because a significant part of the Polaris Flare does not contain bright cores. As seen in Fig. 2, the RHT produces a visualization of filamentary structures irrespective of brightness. This enables us to apply DisPerSe to the RHT backprojection image and obtain a representative skeleton of the *Herschel* image to use as input to FiLTER.

The distribution of filament widths in the *Herschel* image is shown in Fig. 6. The distribution has a peak at 0.06 pc and a spread of $\sigma_w = 0.04$, twice as much as the typical error in the width determination (σ_{fit}) in our implementation of the code. The intrinsic spread of the distribution is: $\sigma_{\text{int}} = (\sigma_w^2 - \sigma_{\text{fit}}^2)^{1/2} = 0.035$ pc. Though lower than the characteristic width of 0.1 pc (e.g. Arzoumanian et al. 2011; Koch & Rosolowsky 2015), the peak value found here falls within the spread of the distributions from these works.

We investigate whether there are trends in the distribution of widths across the cloud, by constructing a smoothed map of the widths found by FiLTER (Fig. 7). We use a boxcar filter of the same size as the maps in Fig. 4 (5', or 0.2 pc) to allow for a better visual comparison. The map shows fluctuations in the width of filaments that do not appear to have any large-scale systematic trend. This remains the case for maps with smaller smoothing kernels. However, when comparing the distribution of widths within region A (Fig. 8, left, dotted red line) to that of the rest of the map (solid black line), we find that the former is slightly shifted towards lower values. A KS test rejects the hypothesis that the two originate from the same parent distribution at the 0.001 level. In constructing the distributions we discard structures with lengths less than 0.2 pc, as these have too small aspect ratios to be considered filamentary. There is an indication that the

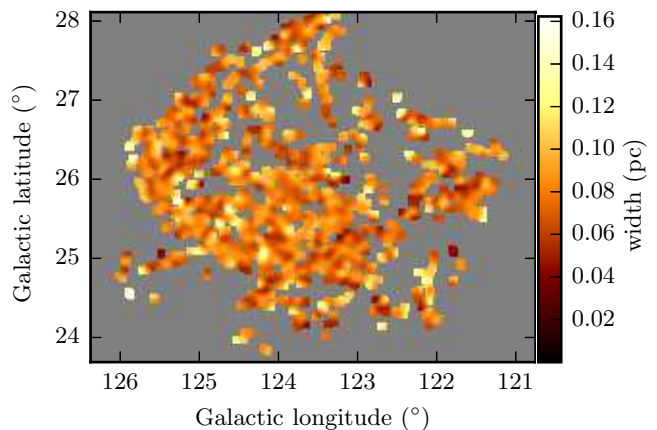


Figure 7. Map of filament widths found with FiLTER, smoothed with a 5' boxcar filter.

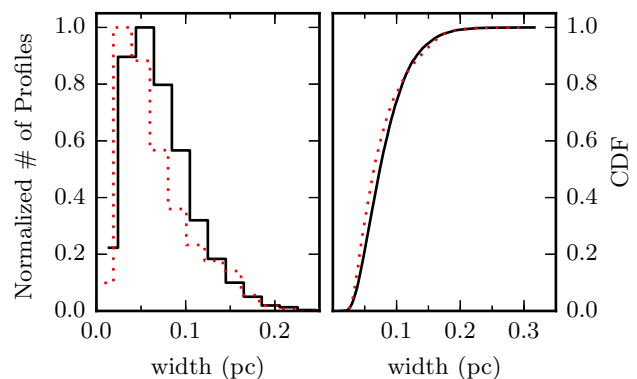


Figure 8. Left: Normalized distribution of widths found with FiLTER in the entire map (solid black) and in region A (dotted red) for all structures longer than 0.2 pc. Right: CDF of the same distributions.

shift towards lower widths becomes more pronounced as we raise this threshold to 0.4 pc.

2.4 Analysis of regions A (striations) and B (MCLD123)

Having explored the various observed properties of the cloud and their variation across the map, we now focus on the two regions of interest defined in Fig. 1.

2.4.1 Region A (striations)

Region A contains striking features both in dust emission (appendix of Miville-Deschênes et al. 2010) and in polarization (Fig. 1). Both B_{pos} and striation orientations throughout the area are ordered. This is apparent in the distribution of polarization angles shown in panel (a) of Fig. 9. The distribution of θ resembles a normal distribution with a mean at -20° and a standard deviation of $\delta\theta_{\text{obs}} = 11^\circ$. The mean observational error (panel b) is 7.6° while the 80th percentile of the distribution is 10° . Therefore, a significant contribution to the observed spread is due to the measurement error.

In addition to this uniformity, the mean directions of

⁴ The code is available at: <https://bitbucket.org/ginpan/filter>

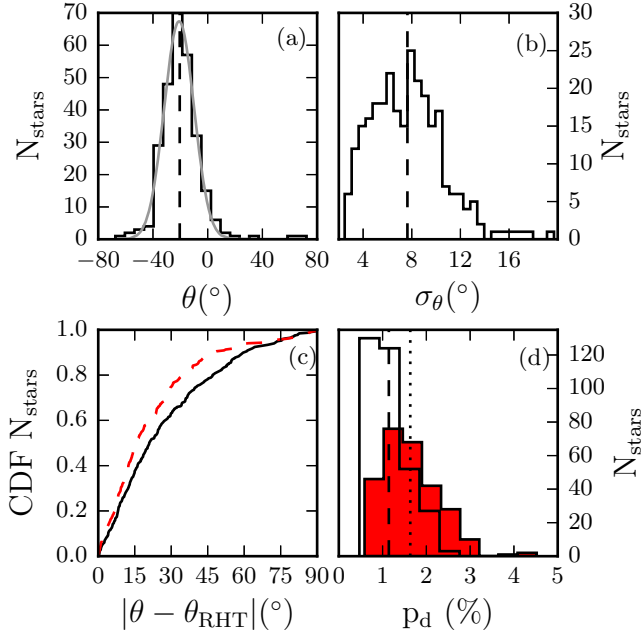


Figure 9. (a): Polarization angle distribution in region A (black solid), Gaussian fit (gray), average (dashed). (b) Distribution of polarization angle measurement errors in region A (solid) and mean (dashed). (c) Normalized CDFs of relative orientations of polarization measurements and dust striations in region A (dashed red) and the rest of the map (solid black). (d) Distributions of p_d in region A (filled red) and the rest of the map (empty black), dashed and dotted lines are their average values.

the field and dust structures appear to be aligned and this occurs to a greater extent than in the rest of the map. This is supported by the comparison of the normalized CDFs of $|\theta - \theta_{\text{RHT}}|$ shown in Fig. 9, panel (c). Inside the region (dashed red line) 75% of the differences $|\theta - \theta_{\text{RHT}}|$ lie in the range $[0^\circ, 30^\circ]$, whereas outside (solid black) only 63% are in the same range.

Another characteristic of region A is that it exhibits a higher fractional linear polarization than the rest of the map, as seen in panel (f) of Fig. 4. We compare the distribution of p_d in region A (filled red) and in the rest of the map (black empty) in panel (d) of Fig. 9. It is clear that p_d in the region extends to higher values than out of the area, and that the mean p_d (dashed line: out, dotted line: in) is lower outside the region.

2.4.2 Region B (MCLD123)

Region B shows a rather different picture than region A. In this area, which is the densest part of the cloud, the plane-of-the-sky field seems to bend along the MCLD123 filament. The left panel of Fig. 10 shows the distribution of θ for this region while the right panel shows the distribution of relative orientations, $|\theta - \theta_{\text{RHT}}|$, for region B (filled red) and the rest of the map (empty black). The mean of the distribution of θ is 90° , and the standard deviation is 25° . The spread is partly due to the large-scale curvature of B_{pos} in the vicinity and on the MCLD123 filament. The values of $|\theta - \theta_{\text{RHT}}|$ show a slight preference for alignment, although they extend to angles consistent with orthogonality.

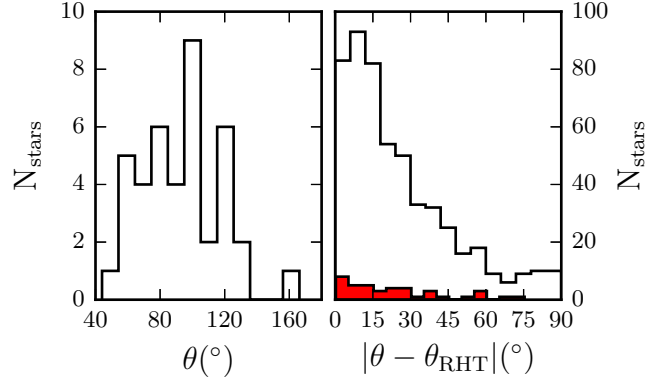


Figure 10. Left: distribution of polarization angles in region B. Right: distribution of $|\theta - \theta_{\text{RHT}}|$ for region B (filled red) and the rest of the map (empty black).

2.5 Magnetic field strength and comparison to Turbulence

The role of the magnetic field in the two regions discussed above can be investigated further by estimating the strength of the plane-of-the-sky magnetic field and by comparing the magnetic energy to that of turbulent motions.

Polarization measurements can be used to estimate the strength of B_{pos} under the assumption that the polarization angle dispersion ($\delta\theta$) is caused by the action of hydromagnetic waves perpendicular to the (mean) magnetic field (Davis 1951; Chandrasekhar & Fermi 1953) (DCF). Based on the idea that a strong field will resist distortion and therefore, $\delta\theta$ will be small, DCF derive:

$$B_{\text{pos}} \approx \sqrt{4\pi\rho} \frac{\delta v}{\delta\theta}, \quad (3)$$

where ρ is the volume mass density of the gas and δv is the velocity dispersion perpendicular to the observed field (along the line-of-sight). The last quantity, $\delta\theta$, can be expressed as the ratio of the (root-mean-squared) turbulent component of the magnetic field ($\langle B_t^2 \rangle^{1/2}$) to the ordered component (B_0) (Hildebrand et al. 2009):

$$\delta\theta \approx \frac{\langle B_t^2 \rangle^{1/2}}{B_0}. \quad (4)$$

2.5.1 The turbulent-to-ordered field ratio

Following Hildebrand et al. (2009) an estimate of the relative strength of B_0 with respect to $\langle B_t^2 \rangle^{1/2}$ can be obtained by calculating the dispersion function of the polarization angles, defined as:

$$\langle \Delta\theta^2(l) \rangle_{\text{tot}} = \frac{1}{N(l)} \sum_{i=1}^{N(l)} \Delta\theta_i^2(l) \quad (5)$$

where the angle differences of all (unique) pairs of polarization measurements, $\Delta\theta_i(l)$, are binned according to the angular distance l in bins containing $N(l)$ pairs. The angle difference of the i^{th} pair, is simply the difference between the polarization angle measured at the position x_i and that at $x_i + l$: $\Delta\theta_i(l) = \theta(x_i) - \theta(x_i + l)$. We constrain $\Delta\theta_i(l) \in [0^\circ, 90^\circ]$. The dispersion function, corrected for the

scatter induced by measurement errors (σ_M), is expected to follow the equation:

$$\langle \Delta\theta^2(l) \rangle_{\text{tot}} - \sigma_M^2 \simeq m^2 l^2 + b^2 (1 - e^{-l^2/2\delta^2}), \quad (6)$$

as shown by Houde et al. (2009) (their equation 44 adapted for optical polarimetry data by Franco, Alves & Girart 2010). In equation 6, δ is the correlation length of B_t , b and m are constants of proportionality, and $\sigma_M^2(l)$ is found according to the equation:

$$\sigma_M^2(l) = \frac{1}{N(l)} \sum_{i=1}^{N(l)} \sigma_{\Delta\theta_i(l)}^2, \quad (7)$$

where $\sigma_{\Delta\theta_i(l)}$ results from error propagation. Equation 6 is expected to hold for distances smaller than the typical scale (d) for large scale variations in B_0 . The parameter b is related to the ratio of the rms B_t to B_0 by:

$$b^2 = \frac{2}{\mathcal{N}} \frac{\langle B_t^2 \rangle}{B_0^2}, \quad (8)$$

where \mathcal{N} is the number of turbulent cells along the line-of-sight:

$$\mathcal{N} \simeq \frac{s_{\text{los}}}{\sqrt{2\pi}\delta}, \quad (9)$$

and s_{los} is the line-of-sight dimension of the cloud.

We implement the method of Hildebrand et al. (2009) and Houde et al. (2009) (H09) in regions A and B. We calculate the dispersion function $\langle \Delta\theta^2(l) \rangle_{\text{tot}}$, as explained above, correct it to obtain the left side of equation 6 and fit the function on the right side of equation 6 to these values with respect to l^2 . The fit takes into account the error of $\langle \Delta\theta^2(l) \rangle_{\text{tot}}$. In Fig. 11 we plot $\langle \Delta\theta^2(l) \rangle_{\text{tot}} - \sigma_M^2$ with distance, l , for each region (black solid lines). The black dots in Figure 11 show the values used for the fit. The fits $p(l) = m^2 l^2 + b^2 (1 - e^{-l^2/2\delta^2})$ are shown with red dashed lines. The distances are shown on a logarithmic scale (the bins used for fitting were linear). The bin size in region B (1.5') was chosen so that there were more than 10 points per bin (in the fitting range). The bin size (1.7') for region A was the minimum that produced a positive value of $\langle \Delta\theta^2(l) \rangle_{\text{tot}} - \sigma_M^2$ for the first bin. A choice of bin size larger by up to 38% in region A and 33% in region B, produces values of b and δ within the error of the fit. The fits were done considering only distances smaller than the scale at which B_{pos} varies ($l < d$). In region A we performed the fits up to $l \approx 20'$. In region B we fit the data up to $l \approx 13'$. The choice of d is that which permits the maximum number of bins to be used in the fit while providing a fit that traces the exponential cut-off as well as possible. In region A both b and δ remain within the error of the fit for a choice of d in the range 8' – 25'. The same holds for region B in the range 9' – 13'.

The results of the fits are shown in the top left of the panels in Fig. 11. The correlation length of B_t is not well constrained, as only in the first bin of region A the effect of the exponential decay in equation 8 is apparent. The values for δ obtained for both regions are consistent within the errors of the fits. Inserting the value for b and δ from the fits into equation 8 we obtain estimates for the ratio $\langle B_t^2 \rangle^{1/2}/B_0$: 0.2–0.5 for region A and 0.3–0.8 for region B. The line-of-sight depth of each region used for these estimates is presented and discussed in the next section.

Within our adopted uncertainties, the ratios in both regions are less than 1. This indicates that the magnetic field is much stronger than the turbulent component in region A and at most comparable to the turbulent component in region B. Moreover, equation 3 can be written as:

$$\frac{\langle B_t^2 \rangle^{1/2}}{B_0} \simeq \frac{\delta v}{v_A} \quad (10)$$

(Hildebrand et al. 2009), where $v_A = B_0/\sqrt{4\pi\rho}$ is the Alfvén speed and δv the velocity dispersion perpendicular to the mean field. From this we can conclude that turbulent motions are most likely sub-Alfvénic in region A and could be sub- to trans-Alfvénic in region B. This is consistent with the conclusion of Hily-Blant & Falgarone (2007) that the magnetic field is dynamically important in region B. These authors found that motions in MCLD123 are trans-Alfvénic, using the dispersion of position angles of diffuse ^{12}CO filaments.

2.5.2 The strength of the ordered component

Having inferred the value of $\delta\theta$ from the H09 method, we now move on to find the values of the remaining quantities that enter into equation 3 and use them to obtain an estimate for B_{pos} in both regions. We present the values used in obtaining these estimates in Table 1.

The gas mass density is equal to: $\rho = \mu m_{\text{H}} n_{\text{H}}$, where m_{H} is the mass of the hydrogen atom, $\mu = 1.36$ is a factor that accounts for the fraction of helium and n_{H} is the total hydrogen number density. The total n_{H} must be used and not n_{H_2} because even though the cloud is molecular, the fraction of gas that is in atomic form may be important ($N_{\text{HI}} \sim N_{\text{H}_2}$ Hily-Blant & Falgarone 2007). To estimate the density in region B, we assume that MCLD123 has a cylindrical geometry. This implies a line-of-sight dimension of $\sim 0.25 - 0.5$ pc, where the lower bound is twice the observed extent of the dense part of the filament and the upper bound is found including the more diffuse parts. The average N_{H_2} from the map of André et al. (2010) is $8 \times 10^{20} \text{ cm}^{-2}$, corresponding to an $N_{\text{H}} \sim 2.4 \times 10^{21} \text{ cm}^{-2}$. Dividing by the assumed line-of-sight dimension gives $n_{\text{H}} \simeq 1500 - 3100 \text{ cm}^{-3}$ (see also Grossmann et al. 1990).

We can obtain a loose constraint on the mean density of region A by arguing that it is likely to be less than that of region B (since the latter contains cores). An upper bound would therefore be $n_{\text{H}}^{\text{A}} < n_{\text{H}}^{\text{B}}$. A lower limit on the density can be estimated by considering existing measurements of n_{H} from UV data of stars in diffuse sightlines. A set of measurements from various works has been collected by Goldsmith (2013) who shows that most sightlines with $N_{\text{H}} \gtrsim 10^{21} \text{ cm}^{-2} \Rightarrow N_{\text{H}_2} \gtrsim 3 \times 10^{20} \text{ cm}^{-2}$ have measured densities: $300 \text{ cm}^{-3} \gtrsim n_{\text{H}} \gtrsim 60 \text{ cm}^{-3}$ (assuming $N_{\text{HI}} \simeq N_{\text{H}_2}$). The column density in region A is estimated⁵ by $N_{\text{H}}^{\text{A}} \simeq N_{\text{H}}^{\text{B}} I_{250}^{\text{A}}/I_{250}^{\text{B}} \simeq 1.2 \times 10^{21} \text{ cm}^{-2}$, where we have assumed that the temperature distribution is quasi-uniform throughout the cloud (Men'shchikov et al. 2010; Schneider et al. 2013) so that intensity (I_{250}) variations

⁵ this is consistent with the value obtained by converting the mean A_V to N_{H} according to Bohlin et al. (1978): $N_{\text{H}} = 1.9 \times 10^{21} A_V (\text{cm}^{-2}/\text{mag})$ for $R_V = 3.1$ (e.g. Savage & Mathis 1979)

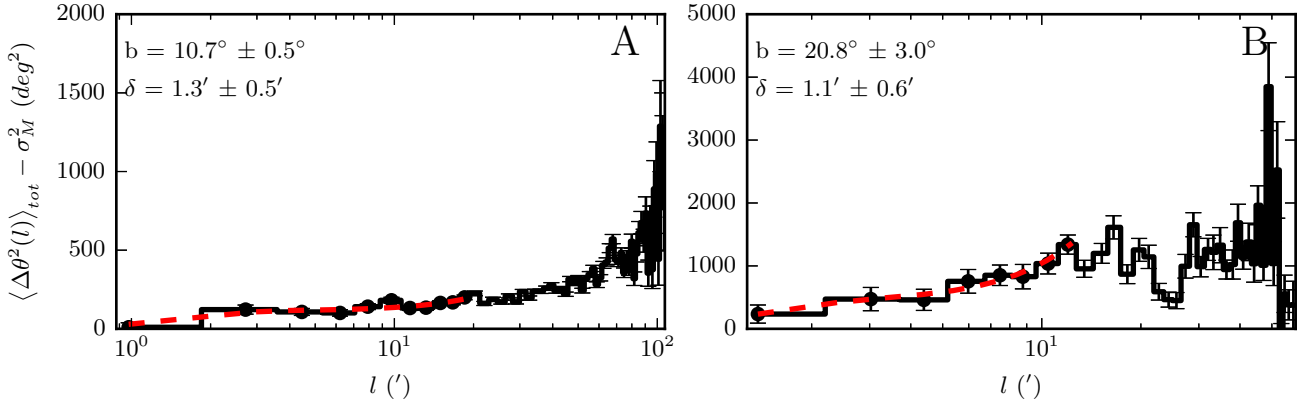


Figure 11. The dispersion function (corrected for measurement errors) vs. angular distance, l , for region A (left) and B (right). The red dashed line shows the best fit function of the form $\langle \Delta\theta^2(l) \rangle_{tot} - \sigma_M^2 = m^2 l^2 + b^2(1 - e^{-l^2/2\delta^2})$. The black dots show the data points that were used in the fits. The fit results for b and δ are shown in the top left.

in the *Herschel* image are mostly caused by N_H fluctuations. Since the Polaris Flare is a molecular cloud, we reason that $n_H^A > 300 \text{ cm}^{-3}$ (the upper limit from the aforementioned sightlines) is an appropriate approximation. The line-of-sight dimension of region A is then ($s_{los} = n_H^A/N_H^A$) $1.3 \text{ pc} \gtrsim s_{los} \gtrsim 0.2 \text{ pc}$. The upper limit is approximately one third of the size of the region as projected on the sky, while the lower limit is similar to the assumed s_{los} in region B. We expect that the true s_{los} lies mostly near the lower limit of this range, because due to the translucent nature of the cloud, the line-of-sight dimension should not be very large. Studies of cirrus clouds in general find a high likelihood of them being sheet-like (e.g. Gillmon & Shull 2006). Along with the fact that regions A and B have similar mean A_V (Table 1), this implies that s_{los} in the two regions should not vary by orders of magnitude.

To estimate the velocity dispersion, δv , we use the ^{12}CO ($J = 1 - 0$) data from the survey of Dame, Hartmann & Thaddeus (2001)⁶. The data, first presented by Heithausen et al. (1993), cover 134 deg^2 including the *Herschel*-mapped area. The angular resolution is $8.7''$ and the spectral resolution is 0.65 km s^{-1} . We fit a Gaussian to the mean spectrum of each region and relate its FWHM (ΔV) to the velocity dispersion (δv) with: $\delta v = \Delta V/(2\sqrt{2\ln 2})$. Complications may arise when the ^{12}CO ($J = 1 - 0$) is used to estimate the velocity dispersion if the line is optically thick. However, Hily-Blant & Falgarone (2007) found that the ^{12}CO ($J = 1 - 0$) line is optically thin in diffuse gas within the MCLD123 filament with column density derived from the scaling of CO to ^{13}CO velocity-integrated line temperatures: $N_{H_2} \sim 10^{20} \text{ cm}^{-2}$. Since the mean column density in region A is $N_{H_2} \approx 4 \cdot 10^{20} \text{ cm}^{-2}$ ($N_{HI} \approx N_{H_2}$) this indicates that the line may also be optically thin within region A. The line is most likely optically thick in the densest parts of region B, however these occupy a very small fraction of the area considered.

The results that follow from equation 3 are presented in Table 1. We show the entire range of values, given the possible variation in the estimated quantities. The range arises

from two factors: the error on δ and the estimate of s_{los} , which enters both in the estimation of the density ρ and the dispersion of polarization angles from the H09 method. The B_{pos} estimates between regions A and B are very similar.

Hily-Blant & Falgarone (2007) obtained an estimate of $B \simeq 15 \mu\text{G}$ for a smaller part of region B, using the angle dispersion of filaments seen in ^{12}CO . This value is 50% that of the lowest bound of our estimate.

B_{pos} with alternative estimate of $\delta\theta$.

We can obtain an alternative estimate of B_{pos} by using the observed angular dispersion $\delta\theta_{obs}$ found in section 2.4.1 from the Gaussian fit to the distribution of polarization angles (see for example section 4.2.3 of Barnes et al. 2015). Ostriker, Stone, & Gammie (2001) applied the DCF method to numerical simulations of MHD turbulence using this type of angle dispersion calculation and found that the method provides a good estimate of B_{pos} when $\delta\theta \lesssim 25^\circ$. They introduced a factor f in equation 3 to correct for line-of-sight averaging: $B_{pos} = f\sqrt{4\pi\rho}\delta v/\delta\theta$ and proposed $f \approx 0.5$.

We use this modification of equation 3 with $\delta\theta_{obs}$ to obtain another estimate of B_{pos} in region A. Because the errors in polarization angle (σ_θ) add to the intrinsic angle dispersion of the cloud, $\delta\theta$, we correct for this bias by (e.g. Crutcher 2004; Girart, Rao & Marrone 2006):

$$\delta\theta^2 = \delta\theta_{obs}^2 - \sigma_\theta^2, \quad (11)$$

where σ_θ is the mean polarization angle error.

The values for the magnetic field strength are shown in the last column of Table 1. They lie within the range of values found using the angle dispersion from H09 and the original equation 3.

3 DISCUSSION

3.1 Properties of the 3D magnetic field

The projected magnetic field of the cloud presents a very inhomogeneous structure. There are regions where it is uniform and others where the measured orientations appear

⁶ Survey online archive: <https://www.cfa.harvard.edu/rtdc/CO/IndividualSurveys/>

Table 1. Values used for estimation of B_{pos} in regions A and B. ΔV : FWHM of CO (J=1-0) line, A_V : average visual extinction (Cambr  sy et al. 2001), N_H : hydrogen column density, s_{los} : line-of-sight dimension, n_H : hydrogen number density, $\delta\theta^{\text{H09}}$: polarization angle dispersion from H09 method (equation 4), $\delta\theta$: polarization angle dispersion from section 2.4.1 (corrected for measurement error according to equation 11), $\langle B_t^2 \rangle^{1/2} / B_0$: turbulent-to-ordered field ratio from H09 method, $B_{\text{pos}}^{\text{H09}}$: plane of sky magnetic field using $\delta\theta^{\text{H09}}$ and equation 3, $B_{\text{pos}}^{\text{mDCF}}$: plane of sky magnetic field using $\delta\theta$ and the modified equation 3 as explained in the text.

Region	ΔV (km/s)	A_V (mag)	N_H $10^{20}(\text{cm}^{-2})$	s_{los} (pc)	n_H (cm^{-3})	$\delta\theta^{\text{H09}}$ ($^\circ$)	$\delta\theta$ ($^\circ$)	$\frac{\sqrt{\langle B_t^2 \rangle}}{B_0}$	$B_{\text{pos}}^{\text{H09}}$ (μG)	$B_{\text{pos}}^{\text{mDCF}}$ (μG)
A	3.1	0.6	12	0.4 – 1.3	300 – 1000	$10^\circ - 29^\circ$	8	0.2 – 0.5	24 – 120	43 – 81
B	2.6	0.7	24	0.25 – 0.5	1500 – 3100	$17^\circ - 44^\circ$		0.3 – 0.8	30 – 111	

random, or significant measurements are entirely absent. These characteristics may provide hints on the nature of the 3D field. Let us consider region A, which has the largest density of significant polarization measurements. As discussed in Paper I, this is not due to variation in stellar density, observing conditions or other systematics. Therefore, region A must be characterized by higher polarization efficiency (in the terminology of Andersson, Lazarian & Vaillancourt (2015): intrinsic polarization per unit column density). We can further investigate this observation by considering that p_d is related to the following factors (Lee & Draine 1985):

$$p_d = p_0 R F \cos^2 \gamma. \quad (12)$$

where γ is the inclination angle (the angle between the magnetic field and the plane-of-the-sky), p_0 reflects the polarizing capability of the dust grains due to their geometric and chemical characteristics, and R is the Reyleigh reduction factor (Greenberg 1968) which quantifies the degree of alignment of the grains with the magnetic field. F accounts for the variation of the field orientation along the line-of-sight and is equal to $F = \frac{3}{2}(\langle \cos^2 \chi \rangle - \frac{1}{3})$, where χ is the angle between the direction of the field at any point along the line-of-sight and the mean field direction. The angular brackets denote an average along the line-of-sight. The increased p_d of region A could therefore be the result of any of these factors (or some combination of them), in other words region A could have:

- i) increased alignment efficiency (e.g. more background radiation, a larger amount of asymmetric dust grains, larger grain sizes), i.e. higher factors p_0 and/or R ,
- ii) more uniform magnetic field along the line-of-sight, i.e. higher F ,
- iii) increased B_{pos} (inclination of B is larger with respect to the line-of-sight), i.e. higher $\cos \gamma$.

Several pieces of evidence challenge the validity of case (i). First, if the radiation illuminating region A were much different in intensity or direction, then the dust temperature of the area would have to be qualitatively different (higher) than in other regions of the cloud. As mentioned in section 2.5, the results from Men’shchikov et al. (2010) imply that temperature and density variations are subtle across the field. Indeed, the temperature PDF presented by Schneider et al. (2013) is narrow. Also, the most likely candidate for providing illumination to the cloud, due to its likely proximity, is Polaris (the star). Zagury et al. (1999) concluded by studying optical and $100 \mu\text{m}$ light from MCLD123, that the star cannot be the primary source of dust heating. Additionally,

larger amounts of (aligned) grains would imply larger column densities (or A_V) than the rest of the cloud, which is not a characteristic of region A. To the best of our knowledge, evidence for significant variation of grain size within the same cloud between regions of such similar A_V does not exist.

We now investigate whether the observed difference in p_d between region A and other parts of the cloud could arise from differences in the properties of the magnetic field along the line-of-sight. We can obtain an upper limit on the influence of the factor F on p_d by keeping all other factors in equation 12 constant and taking the ratio of two regions, for example A and B:

$$\frac{p_A}{p_B} \approx \frac{\langle \cos^2 \chi_A \rangle - \frac{1}{3}}{\langle \cos^2 \chi_B \rangle - \frac{1}{3}} \quad (13)$$

where the average p_d in regions A and B are equal to $p_A = 1.63$, $p_B = 1.3$ and $\langle \cos^2 \chi_i \rangle$ ($i = A, B$) is an average over all lines of sight in region i . For region A, the angle dispersion is small ($\delta\theta \sim 10^\circ$, section 2.4), so we can make the approximation $\langle \cos^2 \chi_A \rangle \approx \cos^2 10^\circ$ (to better than 10%). We check what values of $\langle \cos^2 \chi_B \rangle$ produce the observed ratio of p_A/p_B (within 30%) by drawing $\mathcal{N} = 1 - 9$ angles (the number of turbulent cells in region B) from a normal distribution with $\sigma = 10^\circ - 50^\circ$. After repeating the process 100 times, we find that the most likely σ that can reproduce the observed p_A/p_B are in the range $10^\circ - 25^\circ$, similar to the observed angle dispersion on the plane-of-the-sky (section 2.5). Therefore, it is possible that region A has a more ordered field along the line-of-sight compared to other regions.

Finally, if the 3D orientation of the magnetic field is mostly in the plane-of-the-sky in region A and less so in other parts of the cloud, this could also explain the increased measurement density in this region. We can estimate the change in angle that is needed to obtain the difference in p_d between regions A and B, from equation 12. Taking all factors equal between the two regions except the inclination angle, the ratio of p_d is: $p_d^A/p_d^B = 1.63/1.3 = \cos^2 \gamma_A / \cos^2 \gamma_B$. This ratio could arise either from a pair of large γ_A, γ_B with a small difference or from small angles having a large difference. This ambiguity can be lifted by considering the expected polarization angle dispersions for different inclinations of the magnetic field, studied with MHD simulations by Falceta-Gon  alves et al. (2008). In their work, these authors found that in the range $0^\circ - 60^\circ$ the predicted polarization angle dispersions are below 35° for their model with a strong magnetic field (Alfv  n Mach number 0.7). Since the angle dispersions in the two regions are significantly lower

Table 2. Distance estimates to the cloud from different references.

Reference	d (pc)	method
Heithausen et al. (1990)	≤ 240	Stellar extinction, nearby clouds
Zagury et al. (1999)	125 ± 25	Association to stars
Brunt et al. (2003)	205 ± 62	Size-linewidth relation
Schlaflly et al. (2014)	390 ± 34	Stellar extinction

than this value, it is safe to assume that $0^\circ < \gamma_A, \gamma_B < 60^\circ$. For this range, we find that the observed ratio of p_d can be explained by inclination differences most likely in the range $\gamma_B - \gamma_A = 6^\circ - 30^\circ$. In order to explain the difference in p_d between region A and the lowest mean- p_d region in the map (Fig 4, panel f, approximately at the center of the map) which has a $p_d \sim 0.7\%$, the difference in inclination angle needs to be $20^\circ - 50^\circ$.

With the existing set of measurements, we are not able to conclude whether the variations in polarization fraction are mostly due to change in inclination or due to differences in the uniformity of the field along the line-of-sight. We have, however, provided bounds on the areas of the parameter space in which these differences are likely to occur.

3.2 Cloud distance

In the literature there is no definitive consensus on the cloud's distance. The existing estimates are shown in table 2 along with the method that was used to obtain each one.

Heithausen et al. (1990) base their distance estimate on reddening estimates of stars in the field from Keenan & Babcock (1941), who found reddened stars from distances as close as 100 pc and that all stars farther than 300 pc were reddened. Knowing that Polaris (the star) showed dust-induced polarization, and that the then existing distance estimates to the star were 109 - 240 pc they placed the cloud at a distance $d < 240$ pc. This distance fits with the smooth merging of the cloud at lower latitudes with the Cepheus Flare, at 250 pc.

Zagury et al. (1999) compared IRAS 100 μm emission with optical images of MCLD123 and found that the brightness ratios are consistent with Polaris (the star) being the illuminating source of the cloud in the optical. They placed the cloud at a distance 6 - 25 pc in front of the star ($105 \text{ pc} < d < 125 \text{ pc}$ from the sun) so that its contribution in dust heating would be minimal compared to the interstellar radiation field.

Brunt et al. (2003) used Principal Component Analysis (PCA) of spectral imaging data to infer distances based on the universality of the size-linewidth relation for molecular clouds. Their estimate is consistent with both the above estimates.

Schlaflly et al. (2014) used accurate photometry measurements of the Pan-STARRS1 survey and calculated distances to most known molecular clouds. Their estimate for the distance of the Polaris Flare (390 pc), was obtained for lines of sight in the outskirts of the cloud (outside our observed field).

In Fig. 12 (top) we zoom in on the region surrounding

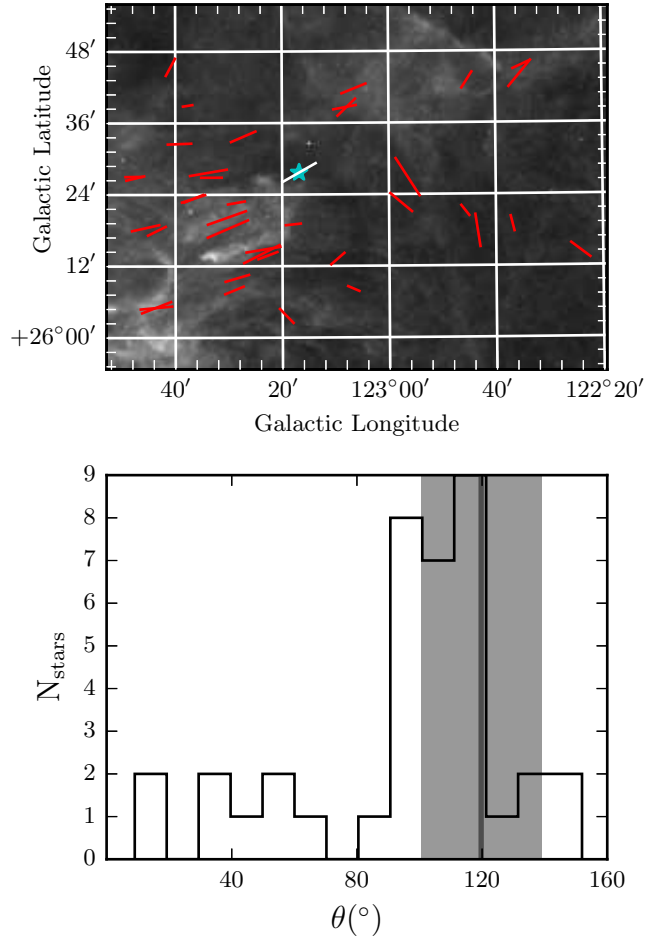


Figure 12. Top: Polarization angle of the star Polaris (Heiles 2000), white segment, compared to our data, red segments. The p_d of Polaris is 0.1%, but has been enhanced 10 times. Its position is marked with a star. Bottom: Distribution of θ in the area shown in the top panel. The dark gray line shows the θ of Polaris while the gray band is the 1σ error. Bin size is 10° .

the North Star and overplot the polarization data (red) and the measurement of the North Star (white) from the Heiles (2000) catalogue on the *Herschel* image. The lengths of the segments are proportional to their p_d , and the length of the Heiles measurement has been enhanced 10 times. The position of the North Star is marked with a blue star. The star happens to be projected on an area of very little dust emission, hence the low p_d . Magnetic field orientations in the area show a strong peak around 110° , with a few measurements (that happen to fall towards the right and bottom of the area) clustering around 40° . This can be seen in the distribution of angles in the area shown in Fig. 12 (bottom). The polarization angle of the North Star (Heiles 2000) is shown with the dark gray vertical line and the light gray band shows the 1σ error. The stars that are nearest to Polaris, in projection, belong to the peak at 100° . The fact that the orientation of the North Star's polarization is consistent with this peak is intriguing. It could add to the evidence supporting that Polaris is behind the Flare, constraining its distance to the Zagury et al. (1999) estimate. However, since the orientation of stellar polarization shifts

by a substantial amount (60°) in $\sim 20'$, denser sampling of the area is needed in order to ascertain this indication.

4 SUMMARY

We combined RoboPol optical polarization measurements and *Herschel* dust emission data to infer the magnetic field properties of the Polaris Flare. We found that linear dust structures (filaments and striations) are preferentially aligned with the projected magnetic field. This alignment is more prominent in regions where the fractional linear polarization is highest (and the number of significant polarization measurements is largest). This correlation supports the idea that variations in the alignment are partly caused by the projection of the 3-dimensional magnetic field. We investigated the possibility of important spatial variations in the filament widths and found only a slight indication of such an effect. Using the Davis (1951); Chandrasekhar & Fermi (1953) and Hildebrand et al. (2009) methods, we estimated the strength of the plane-of-the-sky field and the ratio of turbulent-to-ordered field components in two regions of the cloud: one containing diffuse striations, and the other harbouring the highest column density filament. Our results indicate that the magnetic field is dynamically important in both regions. Combining our results, we find that differences of 6° – 30° in the magnetic field inclination between two cloud regions can explain the observed polarization fraction differences. This difference can also be explained by a difference in the line-of-sight dispersion of the field of 10° – 25°. Finally, we find that the polarization angles of the North Star (Heiles 2000) and of RoboPol data in the surrounding area favour the scenario of the cloud being in front of the star.

ACKNOWLEDGEMENTS

The authors thank L. Cambr  sy for providing the extinction map and S. Clark and E. Koch for helpful advice on their codes. We also thank D. Blinov, J. Liodakis, R. Skolidis, A. Tritsis and E. Palaiologou for their help throughout the duration of this project. We are grateful to M. Houde for his comments on the manuscript and to P. F. Goldsmith and D. Clemens for useful scientific discussions. We finally thank the anonymous reviewer for their insightful comments which helped significantly improve the manuscript. G.V.P. and K.T. acknowledge support by FP7 through the Marie Curie Career Integration Grant PCIG-GA-2011-293531 “SFOnset” and partial support from the EU FP7 Grant PIRSES-GA-2012-31578 “EuroCal”. This research has used data from the *Herschel* Gould Belt Survey (HGBS) project (<http://gouldbelt-herschel.cea.fr>). The HGBS is a *Herschel* Key Programme jointly carried out by SPIRE Specialist Astronomy Group 3 (SAG 3), scientists of several institutes in the PACS Consortium (CEA Saclay, INAF-IFSI Rome and INAF- Arcetri, KU Leuven, MPIA Heidelberg), and scientists of the *Herschel* Science Center (HSC).

REFERENCES

- Andersson B.-G., Lazarian A., Vaillancourt J. E., 2015, ARAA, 53, 501
- Andr   P., Di Francesco J., Ward-Thompson D., Inutsuka S.-I., Pudritz R. E., Pineda J. E., 2014, Protostars and Planets VI, 27
- Andr   P. et al., 2010, A&A, 518, L102
- Arzoumanian D. et al., 2011, A&A, 529, L6A
- Alves F. O., Franco G. A. P., Girart J. M., 2008, A&A, 486, 13A
- Alves de Oliveira C., 2014, A&A, 568, 98A
- Barnes P., Li D., Telesco C, Tanakul N., Marinas N., Wright C., Packham C., Pantin E., Roche P., Hough J., 2015, MNRAS, 453, 2622
- Bensch F., Leuenhagen U., Stutzki J., Schieder R., 2003, ApJ, 591, 1013
- Bohlin R. C., Savage B. D., Drake J. F., 1978, ApJ, 224, 132
- Brunt C. M., Heyer M. H., V  zquez-Semadeni E., Pichardo B., 2003, ApJ, 595, 824B
- Cambr  sy L., Boulanger F., Lagache G., Stepnik B., 2001, A&A, 375, 999
- Chandrasekhar S., Fermi E., 1953, ApJ, 118, 113
- Chapman N. L., Goldsmith P. F., Pineda J. L., Clemens D. P., Li D., Kr  o M., 2011, ApJ, 741, 21C
- Clark S. E., Peek J. E. G., Putman M. E., 2014, ApJ, 789, 82
- Crutcher R. M., Nutter D. J., Ward-Thompson D., Kirk J. M., 2004, ApJ, 600, 279
- Dame T. M., Hartmann D., Thaddeus P., 2001, ApJ, 547, 792
- Davis, Jr., L. 1951, Phys. Rev., 81, 890
- Falceta-Gon  alves D., Lazarian A., Kowal G., 2008, ApJ, 679, 537
- Fiege J. D., Pudritz R. E., 2000, ApJ, 544, 830
- Franco G. A. P., Alves F. O., Girart J. M., 2010, ApJ, 723, 146
- Franco G. A. P., Alves F. O., 2015, ApJ, 807, 5
- Gillmon K., Shull J. M., 2006, ApJ, 636, 908
- Girart J. M., Rao R., Marrone D. P., 2006, Science, 313, 5788, 812
- Goldsmith P. F. Heyer M., Narayanan G., Snell R., Li D., Brunt C., 2008, ApJ, 680, 428
- Goldsmith P. F., 2013, ApJ, 774, 134
- Goodman A. A., Bastien P., Menard F., Myers P. C., 1990, ApJ, 359, 363
- Gorbikov E., Brosch N., 2014, MNRAS, 443, 725
- Greenberg J. M., 1968, Stars & Stellar Systems, 7, 221
- Grossmann V., Heithausen A., Meyerdierks H., Mebold U., 1990, A&A, 240, 400
- Hall J. S., 1955, Liege Symposium, 543
- Heiles C., 2000, AJ, 119, 923H
- Heithausen A., Thaddeus P., 1990, ApJL, 353, L49
- Heithausen A., Stacy J. G., de Vries H. W., Mebold U., Thaddeus P., 1993, A&A, 268, 265
- Heithausen A., 1999, A&A, 349, L53
- Heitsch F., Zweibel E. G., Mac Low M.-M., Li P., Norman M. L., 2001, ApJ, 561, 800
- Hildebrand R. H., Kirby L., Dotson J. L., Houde M., Vaillancourt, J. E., 2009, ApJ, 696, 567
- Hily-Blant P., Falgarone E., 2007, A&A, 469, 173
- Hily-Blant P., Falgarone E., 2009, A&A, 500, L29
- Houde M., Vaillancourt J. E., Hildebrand R. H., Chitsazadeh S., Kirby L., 2009, ApJ, 706, 1504
- Keenan P. C., Babcock H. W., 1941, ApJ, 93, 64K
- Koch E. W., Rosolowsky E. W., 2015, MNRAS, 452, 3435
- Lee H. M., Draine B. T. 1985, ApJ, 290, 211
- Li H.-B., Fang M., Henning T., Kainulainen J. 2013, MNRAS, 436, 3707
- Malinen J. et al., 2015, MNRAS submitted, arXiv:1512.03775
- Matthews B. C., Wilson C. D., Fiege J. D., 2001, ApJ, 562, 400
- Men’shchikov A. et al., 2010, A&A, 518, L103
- Miville-Desch  nes M.-A. et al., 2010, A&A, 518, L104

- Mouschovias T. C., 1976, *ApJ*, 206, 753
 Myers P. C., 2009, *ApJ*, 700, 1609
 Nakamura F., & Li Z.-Y., 2008, *ApJ*, 687, 354
 Ostriker E. C., Stone J. M., Gammie C. F., 2001, *ApJ*, 546, 980
 Padoan P., Goodman A. A., Draine B. T., Juvela M., Nordland Å. R., Rögnvaldsson O. E., 2001, *ApJ*, 559, 1005
 Palmeirim P. et al., 2013, *A&A*, 550A, 38P
 Panopoulou G. V., Tassis K., Goldsmith P. F., Heyer M., 2014, *MNRAS*, 444, 2507P
 Panopoulou G. V. et al., 2015, *MNRAS*, 452, 715
 Pereyra A., Magalhães A. M., 2004, *ApJ*, 603, 584
 Pilbratt G. L. et al., 2010, *A&A*, 518, L1
 Planck Collaboration et al., 2015, *A&A*, 576, 104
 Planck Collaboration et al., 2015, *A&A*, 576, 105
 Planck Collaboration et al., 2014, *A&A*, in press, arXiv:1409.6728
 Planck Collaboration et al., 2015, preprint, (arXiv:1502.04123)
 Savage B. D., Mathis J. S., 1979, *ARA&A*, 17, 73S
 Schlafly E. F. et al., 2014, *ApJ*, 786, 29S
 Schlegel D. J., Finkbeiner D. P., Davis M., 1998, *ApJ*, 500, 525
 Schneider N. et al., 2013, *ApJL*, 766, L17
 Soler J. D., Hennebelle P., Martin P. G. et al., 2013, *ApJ*, 774, 128
 Sousbie T., 2011, *MNRAS*, 414, 350
 Sugitani K. et al., 2011, *ApJ*, 734, 63S
 van den Bergh, S., 1956, *Z. Ap.*, 40, 249
 Wagle G. A., Troland T. H., Ferland G. J., Abel N. P., 2015, *ApJ*, 809, 17W
 Ward-Thompson D. et al., 2010, *A&A*, 518, L92
 Zagury F., Boulanger F., Banchet V., 1999, *A&A*, 352, 645

This paper has been typeset from a \LaTeX file prepared by the author.